

Simulating the hydrodynamics of stellar explosions followed by a pulsar wind on a moving-mesh

S M Franklin

Department of Physics, University of Bath, Bath BA2 7AY, United Kingdom

E-mail: `smf53@bath.ac.uk`

Abstract. Gamma Ray Bursts (GRBs) are generated after massive stellar explosions when jets of plasma are launched from the stellar remnant. The jet's interaction with an external medium drives synchrotron emission, producing the GRB and an afterglow with frequencies ranging from X-ray to radio. Standard GRB models predict an afterglow flux that rapidly decays according to a power law in time. However, since the launch of the *Neil Gehrels Swift* space observatory in 2004, many afterglows have been found that exhibit a shallow flux decay plateau phase at early times. These plateaus are believed to result from energy injection from a central engine (either a spinning down pulsar wind or matter fallback onto a black hole). In this work, I use a novel moving-mesh relativistic hydrodynamics code to simulate the dynamics of a GRB jet with an initial blast wave followed by a relativistic pulsar wind. I found that such simulations, when combined with a simplified synchrotron emission model, recreated the structure of the observed light curves for GRBs 61007, 60729, and 120213A. Allowing their diverse shapes to be directly explained by differences in the dynamics.

1. Introduction

The most luminous explosions in the universe, Gamma-Ray Bursts (GRBs), are intense flashes of gamma rays detected at cosmological distances. They are believed to be generated by cataclysmic astrophysical events such as the collapse of a very massive star (long GRBs) [1–3] or the merging of a neutron star (NS) with another NS or possibly with a black hole (BH) (short GRBs) [4, 5]. The joint detection of gravitational waves and electromagnetic radiation from GRB170817 famously demonstrated the NS-NS merger scenario in 2017 [6, 7]. These explosions launch collimated ultra-relativistic jets that interact with a circumburst medium and the interstellar medium (ISM), producing the observed gamma-rays and afterglow from X-ray to radio frequencies [8].

GRBs and their afterglows are explained by the classical fireball model [9, 10], which describes the hydrodynamic evolution after an instantaneous injection of mass and energy ($10^{48\text{--}51}\text{erg}$). Initially, the optically thick fireball accelerates as it expands until all of its internal energy is converted to kinetic energy [11]. The fireball then coasts freely, propagating like a pulse of energy at almost the speed of light with a frozen radial profile [12]. The frozen pulse approximation breaks down as the fireball begins to spread. If the fireball is inhomogeneous, it generates internal shocks that produce the observed GRB through synchrotron radiation and inverse Compton scattering [13, 14]. After coasting ends, the fireball follows a self-similar solution first described by Blandford & McKee 1976 [15] (denoted BM76 hereafter) and decelerates by sweeping up matter from the ISM. Swept-up electrons are shock-accelerated and interact with small-scale ($\sim 10^4\text{ -- }10^5\text{cm}$) shock-amplified magnetic fields [16], driving synchrotron radiation [17]. This produces the GRBs afterglow following a power law decay in time [18].

The launch of *Swift* in 2004 [19] revealed early-time plateau phases with shallow flux decay in X-ray afterglow light curves to be more common than initially anticipated. This plateau phase is associated with a central engine injecting energy into the system over an extended period [20, 21]. The

injection method is believed to be either a fallback of matter onto a BH or wind from a spinning down pulsar depending on the stellar remnant [22–24]. For the duration of energy injection, the system is expected to follow a profile described by van Eerten 2014 [25] (vE14 hereafter); the forward shock (FS) from the initial instantaneous injection is followed by a contact discontinuity (CD) separating the material swept up by the FS from the ejecta, as well as a reverse shock (RS) running into the ejecta. The FS and RS contribute to the emission, and either can be dominant [20–22, 26].

In this work, I investigate the spinning-down pulsar scenario to verify the resulting GRB light curves align with observed GRBs with a plateau phase. Several popular models exist explaining the creation of the jets in this scenario, such as a protomagnetar wind [27], hyperaccretion onto the NS [28, 29] or strong toroidal fields floating up through the NS and breaking through its surface [30]. After launching the jets and cooling, the magnetar ejects a cold Poynting-flux-dominated outflow that remains near-isotropic at first and decays after the magnetar spins down [22]. To numerically simulate this, I use the newly developed moving-mesh special relativistic hydrodynamics (SRHD) code, GAMMA [31], to simulate the evolution of the jets. GAMMA allows for better numerical accuracy and computational efficiency than other simulations out to trans-relativistic times by taking an arbitrary Lagrangian-Eulerian (ALE) approach and implementing local cooling [31, 32]. By combining several simulations with a simplified synchrotron emission model, afterglow light curves are recreated. The features of these are explained using the description of the dynamics from simulations. The resulting light curves are compared to several observed GRB light curves to investigate if the same dynamical description could apply to them.

The GAMMA code and the simulation setups are described in section 2. The dynamical evolution of these simulations is discussed in section 3. The emission model and resulting light curves are described and discussed in section 4.

2. Numerical Methods

2.1. Relativistic Hydrodynamics on a moving-mesh

GAMMA’s moving-mesh ALE approach in the direction of fluid flow allows for efficient simulations with high resolution. This is crucial for describing the complex system of shocks travelling at relativistic speeds being investigated.

The numerical approach to dynamics is the same as in Lamberts and Diagne 2018 [33], and Ayache et al. 2020 [32] (LD18 and AvED20 hereafter), which I describe here. GAMMA solves the following system of conservation equations in spherical coordinates (r, θ, ψ) in one dimension (1D):

$$\partial_t \mathbf{U} + \nabla \mathbf{F}(\mathbf{U}) = \mathbf{S}, \quad (1)$$

where \mathbf{U} is the vector of *conserved variables*, $\mathbf{F}(\mathbf{U})$ is the corresponding flux vector, \mathbf{S} is the source term and ∇ is the divergence operator cast onto all of $\mathbf{F}(\mathbf{U})$ ’s spatial vector components. Expressed in terms of primitive variables \mathbf{U} and $\mathbf{F}(\mathbf{U})$ are:

$$\mathbf{U} = \begin{pmatrix} D \\ m \\ \tau \end{pmatrix} \equiv \begin{pmatrix} \rho\Gamma \\ \rho h\Gamma^2 v \\ \rho h\Gamma^2 - p - D \end{pmatrix} \begin{array}{l} \text{(Rest-mass density)} \\ \text{(Momentum)} \\ \text{(Energy)} \end{array}, \quad (2)$$

$$\mathbf{F}(\mathbf{U}) = \begin{pmatrix} Dv \\ mv + p \\ m \end{pmatrix}, \quad (3)$$

where ρ, p and \vec{v} are the primitive variables: rest-mass density and pressure in the co-moving frame and fluid velocity in the lab frame, respectively. h is the specific enthalpy (including rest-mass energy) in the co-moving frame, $\Gamma = (1 - (v/c)^2)^{-1/2}$ is the Lorentz factor with the speed of light set to $c = 1$. In 1D, the spherical coordinates formulation of these equations requires the inclusion of the non-zero geometric source term $\mathbf{S} = (0, 2p/r, 0)^T$ where r is the radius measured from the central engine.

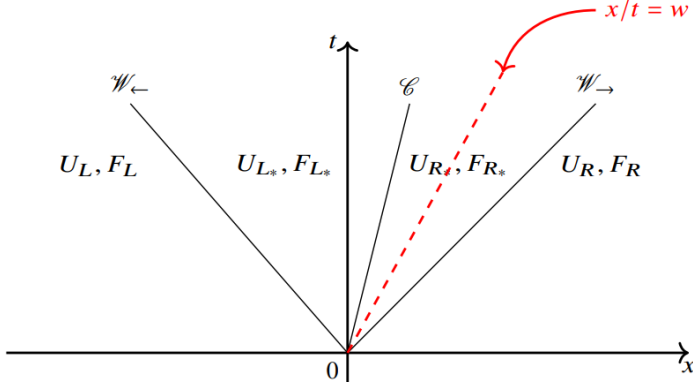


Figure 1. Schematic representation of a Riemann problem from Ayache et al. 2022 [31]. Shows the interface between two cells, with three waves (\mathcal{W}_- , \mathcal{C} , \mathcal{W}_+) emerging from the CD that split the fluid into four regions (L , L_* , R_* , R). $\mathbf{F}_{\text{Riemann}}$ and $\mathbf{U}_{\text{Riemann}}$ are given by selecting the \mathbf{U} and \mathbf{F} of the region the red line w lies within. The flux across the interface is given by $\mathbf{F} = \mathbf{F}_{\text{Riemann}} - w\mathbf{U}_{\text{Riemann}}$, with the second term correcting for the motion of the interface.

The equations are closed using the equation of state for an ideal monoatomic fluid:

$$p(\rho, \epsilon) = \rho\epsilon(\hat{\gamma} - 1), \quad (4)$$

where ϵ is the specific internal energy density, and $\hat{\gamma}$ is the adiabatic index, which is set to be $\hat{\gamma} = 4/3$ for the ultra-relativistic case. As in LD18, a passive scalar s is included to distinguish between different fluid regions. This scalar follows $S = s\rho\Gamma$ in the lab frame and $F = \rho sv\Gamma$ for its flux.

The simulations consist of a grid of N cells along the r direction with $(N-1)$ interfaces between them. GAMMA uses the Harten-Lax-van Leer-Contact (HLLC) Riemann solver [34], which finds the flux at each interface at a given time by solving a Riemann problem for them. An example of a Riemann problem can be seen in figure 1. The ALE approach allows interfaces to move at an arbitrary velocity (less than c). This velocity is set equal to the CD velocity in the Riemann problem at each interface.

2.2. Simulation Setup

Simulations are set up using a similar approach to LD18 and AvED20. Firstly the initial blast wave is set up running into the ISM as a self-similar profile described by BM76 (I will use BM solution to refer to this) resulting from the instantaneous injection of energy $E_{\text{BM}} = 10^{53}$ erg. To emulate the behaviour of the central engine, cold ejecta with Lorentz factor $\Gamma(t)$ is injected into the fluid from the left boundary. This injection takes place for $t_{\text{inj}} = 10^4$ s between $t_0 = 4 \times 10^6$ s and $t_f = t_0 + t_{\text{inj}}$, where time t is measured in the lab frame (i.e. the frame of the unshocked fluid). The total energy injected is set equal to the energy of the initial blast wave $E_{\text{inj}} = E_{\text{BM}}$ so $\dot{E}_{\text{inj}} = E_{\text{inj}}/t_{\text{inj}} = 10^{49}$ ergs $^{-1}$. The ejecta being cold, the pressure is set by $\eta = p/\rho c^2 = 10^{-5}$, where ρ is expressed as a function of E_{inj} and $\Gamma(t)$ as follows:

$$\rho(t) = \frac{\dot{E}_{\text{inj}}}{4\pi r^2(t)v(t)\Gamma^2(t)c^2[1 + \eta(\frac{\hat{\gamma}}{\hat{\gamma}-1} - \frac{1}{\Gamma^2(t)})]}. \quad (5)$$

Since \dot{E}_{inj} is set to be constant and the ejecta is cold, the fluid profile can be described by $\Gamma(t)$ alone. In these simulations, the injection profile is characterised by an initial flat head region with a constant Lorentz factor Γ_0 and a region with decreasing velocity until engine shutdown at t_f with Γ_f . The injection profile is therefore given by:

$$\Gamma(t) = \begin{cases} \Gamma_0 : & t_0 < t < t_\alpha, \\ \Gamma_f + \left(\frac{\Gamma_0 - \Gamma_f}{t_f - t_\alpha} \right) (t_f - t) : & t_\alpha < t < t_f, \end{cases} \quad (6)$$

Table 1. Run parameters

Run	α	λ	Γ_0	Γ_f	Description
run 0	-	-	-	-	no injection
run 1	1	10^{-3}	-	-	BH collapse
run 2	0.5	10^{-3}	100	10	Gradual shutdown with constant \dot{E}_{inj}
run 3	1	10^{-6}	100	-	Gradual shutdown with decaying \dot{E}_{inj}

where $t_\alpha = t_0 + \alpha(t_f - t_0)$ sets the limit between the head and tail regions with $0 < \alpha < 1$. As α increases, the tail region is set to occur earlier in the injection. At $\alpha = 1$, there is no head region; at $\alpha = 0$, there is no tail region; and at $\alpha = 0.5$, the head and tail regions are split equally.

After the injection ends, the boundary conditions are used to reduce ρ and v exponentially with p following according to cold flow:

$$v(t) = v_f e^{-\lambda(t-t_f)}, \quad (7)$$

$$\rho(t) = \rho_f e^{-\lambda(t-t_f)} + \rho_{ISM}, \quad (8)$$

$$p(t) = \eta \rho(t) c^2. \quad (9)$$

Here ρ_f and v_f are the rest mass density and velocity at the time of switch-off, ρ_{ISM} the density of the ISM acting as a floor, and λ is a chosen decay constant.

I run SRHD simulations with $\Gamma_0 = 100$ and various values of α and λ to describe different progenitor scenarios and a run with no injection (reported in table 1). Run 0 represents the case with no injection, acting as a comparison to the BM solution and a benchmark for our results. Run 1 has no tail region and is shutdown quickly $\lambda = 10^{-3}$, representing the scenario with a pulsar emitting an isotropic wind before collapsing into a BH, thus shutting down the wind nearly instantaneously (although an instantaneous shutdown is avoided in our simulations to prevent errors caused by zeroth-order discontinuities). Run 2 has a significant tail region that decreases to $\Gamma_f = 10$ before following the same decay as run 1, representing a pulsar wind with a gradual shutdown leading to a long-lived reverse shock as in AvED20. Run 3 has no tail region and shuts down slowly after t_f , $\lambda = 10^{-6}$, representing a gradual shutdown of \dot{E}_{inj} . This deviates from run 2, where \dot{E}_{inj} remains constant throughout the tail region before switching off suddenly.

The right of the grid uses an outflow boundary, while the left uses the boundaries described above. Simulations start with 8000 cells and use the same adaptive mesh refinement criteria as in AvED20, with the maximum number of cells being 10000. The left boundary moves at $v_{\text{left}} = 0.3$ and the right one with $v_{\text{right}} = 1.3$ to allow for computational efficiency and ensure the blast wave is always in frame.

3. Hydrodynamical evolution

In this section, I investigate the hydrodynamics for each run by observing their fluid profiles at important times and tracking the peak Lorentz factor and pressure throughout. This provides a detailed description of the evolution of the jets that will be used to motivate the emission model and explains the features of the resulting afterglows.

The pressure, rest mass density, and Lorentz factor for each run can be seen in figure 2 at two important times in the lab frame. The first time $t = (4.094 \pm 0.033) \times 10^6$ s (a) is soon after the injection period has ended, and the central engine has begun to shut down. The second time (b) $t = (9.163 \pm 0.094) \times 10^6$ s shows the self-similar profile taken in each run until the engine shutdown is communicated to the RS. Times are measured to the order of $t_{\text{inj}} = 10^4$ s, and the spread in timings between different simulations introduces uncertainty in the times. In both cases. These have been plotted as a function of r/r_{shock} , where r_{shock} is the radius of the initial blast wave measured from the central engine. This allows the dynamics around the FSs, CDs, and RSs to be captured. Both cases show the fluid split into four distinct regions: the ISM ahead of the initial blast wave; the "BM

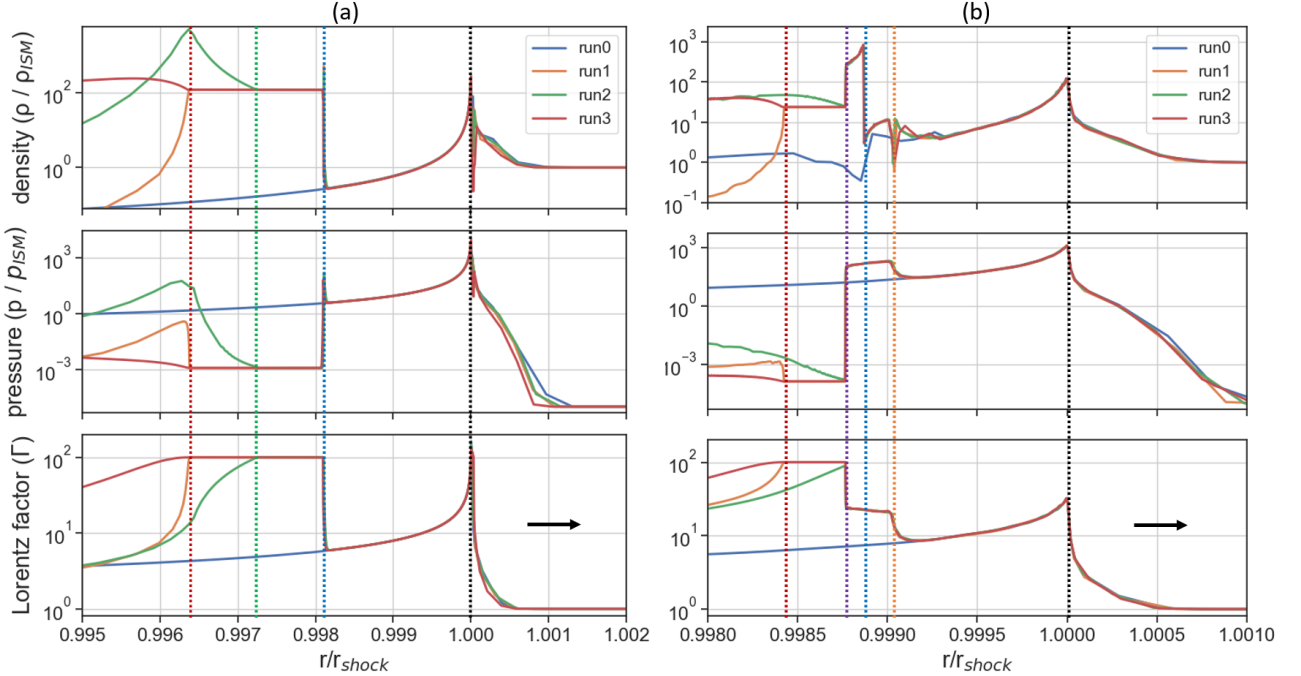


Figure 2. The normalized density ρ/ρ_{ISM} (top), normalized pressure p/p_{ISM} (middle) and Lorentz factor Γ (bottom) profiles for all the runs at lab times $t = (4.094 \pm 0.033) \times 10^6$ s (a), and $t = (9.163 \pm 0.094) \times 10^6$ s (b). In (a), the dotted vertical lines show the positions of the initial blast wave (black), the boundary between the injected fluid and the shocked fluid (blue), the start of the tail region for run 2 (green), and the engine shutdown (red). In (b), the initial blast wave and engine shutdown are shown again (black and red, respectively), and the RS-CD-FS system is at the interface between the injected region and BM region (purple, blue and orange, respectively).

region" that follows a BM solution behind the initial blast wave; the "injection region" separated from the BM region by an RS-CD-FS system; and the "decay region" after the energy injection has ended. For run 2, the injected region is split into two parts, the head and the tail, before and after t_α , respectively, as discussed in section 2. At both times, a numerical error is seen as a sudden dip in the density; this propagates through the system and is likely to have a negligible impact on the results.

The RS-CD-FS system between the BM and injection regions seen at $t = (9.163 \pm 0.094) \times 10^6$ (a) matches the self-similar profile for a blast wave expanding in a homogeneous medium with constant energy injection described in vE14.

In figure 3, the peak Lorentz factor (a) and pressure (b) for the BM region, injection region, and overall are shown for each run. For runs with injection, at early times, the peak Lorentz factor is dominated by the injection region, which remains constant. The sudden drop in Γ indicates the time when the engine shutdown is communicated to the RS and a transition from the self-similar energy injection profile to the instantaneous energy injection profile, as discussed in vE14. In run 2, this drop occurs earlier, instead indicating the time when the tail region of injection is communicated to the RS.

The scenarios outlined in table 1 produce various transition phases. BH collapse (run 1) results in the Lorentz factor of the fluid crossing the RS to decrease to $\Gamma(t) = 1$ essentially instantaneously, causing a rapid transition from the constant energy injection profile to the instantaneous energy injection on the order of the sound crossing time (see vE14). In contrast, a gradual shutdown of the central engine (runs 2 and 3) results in a gradual decrease in the Lorentz factor of the fluid crossing the RS, meaning the transition takes place over an extended period.

The fluid profiles during the transitions are shown for runs 2 and 3 in figure 4 at $t =$

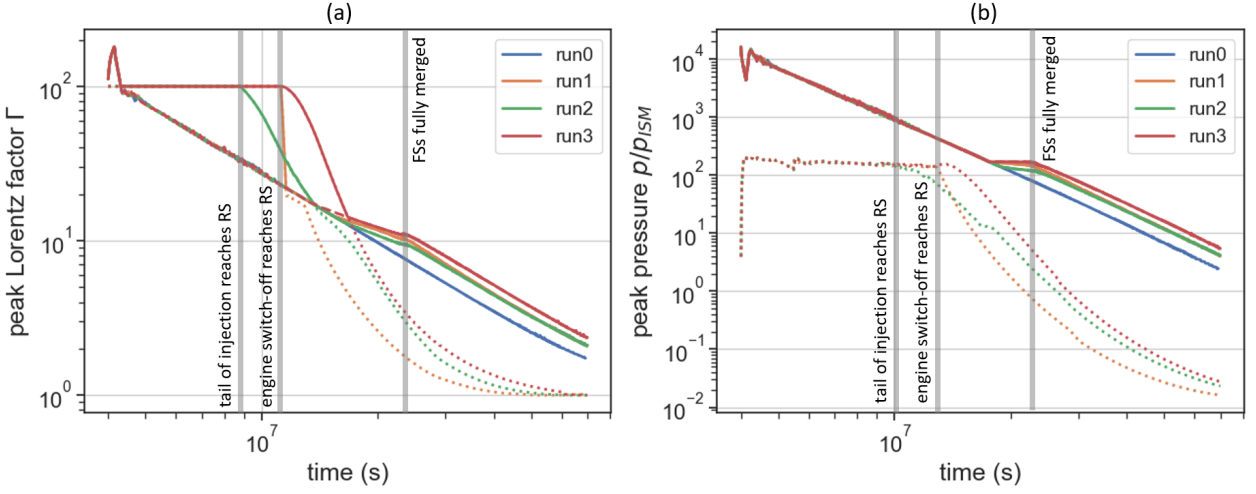


Figure 3. The peak Lorentz factor Γ (a) and peak pressure p (b) throughout the time of the run (in the unshocked fluid frame), overall (solid lines), in the BM region (dashed lines), and the injection region (dotted lines). The grey vertical lines indicate the time at which the tail region of the injection is communicated to the RS, the time at which the engine shutdown is communicated to the RS, and the time when the resulting FS after the transition has fully merged with the initial blast wave.

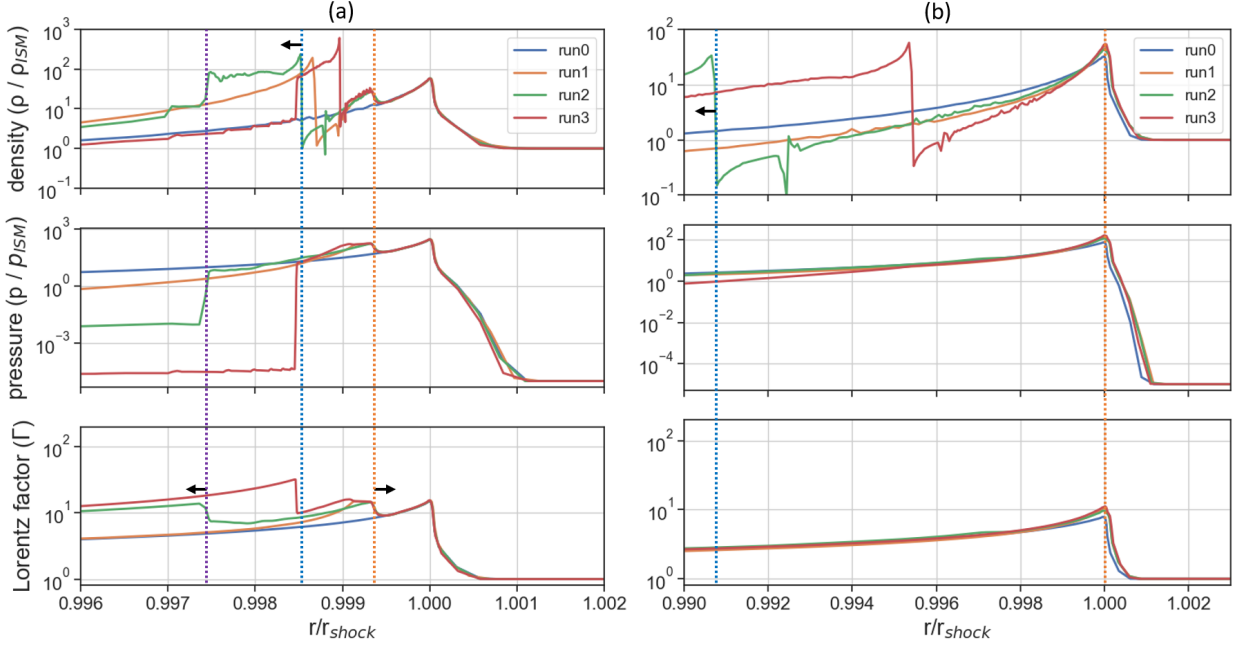


Figure 4. The normalized density ρ/ρ_{ISM} (top), normalized pressure p/p_{ISM} (middle) and Lorentz factor Γ (bottom) profiles for all the runs during the transition phase at lab times $t = (1.479 \pm 0.016) \times 10^7$ s (a) and after the merging of the FSs around $t = (2.271 \pm 0.029) \times 10^7$ s (b). The vertical lines show the RS-CD-FS system for run 2 (purple, blue and orange, respectively). The arrows indicate which direction a discontinuity is moving relative to the initial blast wave; the FS catches up to the FS of the initial blast wave while the CD and RS fall far behind.

$(1.479 \pm 0.016) \times 10^7$ s (a). In each run, the FS of the injected material approaches the initial blast wave while the CD and RS decelerate earlier and fall behind. The effect of the approaching FS is seen in figure 3 when the decay of the peak pressure diverges from run 0 as the FSs merge. After the shocks fully merge, at $t = (2.336 \pm 0.030) \times 10^7$ s (b), the pressure and Lorentz factor continue to

decay parallel to run0 according to BM76. Notably, runs 1 and 2 approach one another in this region while run 3 maintains a higher pressure and Lorentz factor due to the lower decay rate λ , meaning more energy injection overall after the engine is switched off. We discuss the effect of the various transitions and the merging of the FSs on the emission in section 4.

4. Emission

4.1. Simplified emission model

Synchrotron emission is generated by shock-accelerated electrons interacting with small-scale ($\sim 10^4 - 10^5$ cm) shock-amplified magnetic fields and is typically the dominant form of emission in the afterglow phase of the GRB [16, 17]. In this subsection, I describe my treatment of the synchrotron emission theory and its combination with the simulations to reproduce GRB afterglow observations.

The standard approach to the synchrotron theory [9, 35–39] assumes a fraction of the local energy density, e' in the co-moving frame, is in the accelerated electron population, $\epsilon_e \sim 0.1$, and magnetic field, $\epsilon_B \sim 0.01$. Shocked electrons are assumed to be accelerated into a power law distribution of energies with slope $p \sim 2.2$ [40].

I use these assumptions alongside the analytical model outlined in van Eerten et al. 2010 [41] to approximate the observed flux F_v at a frequency v_{obs} for an observer at cosmological distances, facing a jet head-on. In the co-moving frame, the peak spectral power emitted by the shocked electrons is given by

$$P'_{\text{peak}} = 0.88 \left(\frac{16}{3} \right)^2 \frac{p-1}{3p-1} \frac{\sigma_T m_e c^2}{8\pi q_e} n' B', \quad (10)$$

where σ_T is the Thomson cross section, m_e is the electron mass, q_e is the electron charge, n' is the co-moving number density, and $B' = \sqrt{\epsilon_B e' 8\pi}$ is the co-moving magnetic field strength.

The shape of the emission spectrum is determined by the synchrotron critical frequency v_m and the cooling frequency v_c [37, 38, 41]. In the co-moving frame, these frequencies are set according to:

$$v'_m = \frac{3}{16} \left(\frac{p-2}{p-1} \frac{\epsilon_e e'}{n' m_e c^2} \right)^2 \frac{q_e B'}{m_e c}, \quad (11)$$

and

$$v'_c = \frac{3}{16} \left(\frac{3m_e c}{4\sigma_T \epsilon_B e' t / \gamma} \right)^2 \frac{q_e B'}{m_e c}, \quad (12)$$

where γ is the Lorentz factor of the fluid element in the lab frame, used to transform the time t in the lab frame to the time co-moving with the fluid element.

A simplified approach is taken to combine these equations with simulations. The passive scalar, s , described in section 2 splits the fluid at the CD between BM and injection region. At each time step, a shock is detected in both regions as the largest radius where the normalized pressure rises above $p/p_{\text{ISM}} = 1$. The energy density, number density, Lorentz factor, and radius R are approximated as uniform throughout the shocked region. The energy density and number density are taken as averages found throughout the volume behind the shock, which contains a fraction $\xi \sim 0.8$ of the total mass behind it and within the region. Since the Lorentz factor and radius are also used to approximate the shocks Lorentz factor and Radius, these are instead taken as energy-weighted averages within this volume.

These approximations are used with equations 10, 11 and 12, to obtain approximate values of P'_{peak} , v'_m and v'_c throughout both regions at every time step.

The spectral power emitted at a given frequency P'_v is calculated according to the synchrotron

spectrum of a relativistic shock:

$$P'_v = \begin{cases} P'_{\text{peak}}(v'/v'_m)^{1/3} : & v' < v'_m < v'_c, \\ P'_{\text{peak}}(v'/v'_c)^{1/3} : & v' < v'_c < v'_m, \\ P'_{\text{peak}}(v'/v'_c)^{-1/2} : & v'_c < v' < v'_m, \\ P'_{\text{peak}}(v'/v'_m)^{(1-p)/2} : & v'_m < v' < v'_c, \\ P'_{\text{peak}}(v'_c/v'_m)^{(1-p)/2}(v'/v'_c)^{-p/2} : & v'_m, v'_c < v', \end{cases} \quad (13)$$

where v' is the observed frequency translated into the co-moving frame by considering the cosmological redshift, z , at luminosity distance, d_l , and the relativistic Doppler shift from the motion of the shock at velocity β :

$$v' = (1+z)\gamma(1-\beta)v_{\text{obs}}. \quad (14)$$

The observed monochromatic flux generated within the shocked region is calculated by multiplying it by the volume of the expanding jet and accounting for its cosmological distance to the observer [32, 41]:

$$F_v = \frac{1+z}{2d_l^2} \int_0^{2\theta_0} \sin \theta d\theta R^2 \Delta R \frac{P'_v}{\gamma^2(1-\beta)^2}, \quad (15)$$

where axial symmetry has been assumed, the opening angle is taken as $\theta_0 = 2.5^\circ$ [42], and ΔR is the width of the shocked shell (assumed to be small compared to R) calculated as [37, 41]:

$$\Delta R = \frac{1}{1-\beta} \frac{R}{12\gamma^2}. \quad (16)$$

As in vE14, I have taken the cosmological redshift to be $z = 2.23$ (the average *Swift* sample redshift in 2009 [43]) and, therefore, luminosity distance $d_l = 5.6 \times 10^{28}$ cm. The resulting afterglow light curves are calculated in the X-ray band averaged through the $(0.3 - 10)$ keV/ $(7.25 \times 10^{16} - 2.42 \times 10^{18})$ Hz range. The resulting afterglow light curves for each run are shown in figure 5, along with the contributions from the BM and injection regions. Here, the observer time is approximated as

$$t_{\text{obs}} \approx (1+z)(t - R_{\text{BM}}/c), \quad (17)$$

where R_{BM} is the approximated radius of the shocked volume in the BM region.

4.2. Discussion of X-ray light curves

In this subsection, I describe the features for each X-ray light curve in figure 5, explaining them in terms of the simulation dynamics. I compare them to the similar *Swift*-XRT light curves for GRBs 061007, 060729, and 120213A seen in figure 6 to demonstrate how the spinning down pulsar scenario explains observations. Each light curve is described by a series of power laws: $F_v \propto t_{\text{obs}}^{-\kappa}$ for each phase. The estimated timings for each phase of the light curves and the corresponding decay constant κ are detailed in tables 2 and 3, respectively. For observed light curves, the steep initial decay phase has been ignored since simulations begin with the initial blast wave already within the deceleration phase, meaning no initial rapid decay is reproduced.

The light curves for runs 1-3 figure 5 (b-d) all share some common features, most notably the initial plateau phase due to the injection of energy, as seen by the contribution to the flux in the injection region. The BM region's emission becomes dominant once the engine shutdown is communicated to the front of the injection region, meaning the flux from this region decays. For run 1, this happens around $t_{\text{obs}} \sim t_{\text{in}} = 1 \times 10^4$ s; for run 2, this happens earlier around $t_{\text{obs}} \sim t_{\text{in}}/\alpha = 5 \times 10^3$ s due to the tail region of its injection; for run 3, this happens slightly later $t_{\text{obs}} \sim 2 \times 10^4$ s since its engine shutdown has a slower decay rate. In run 1, the sudden injection switch-off causes a brief rapid decay phase followed by a second plateau phase due to the merging of the FS from the injection with

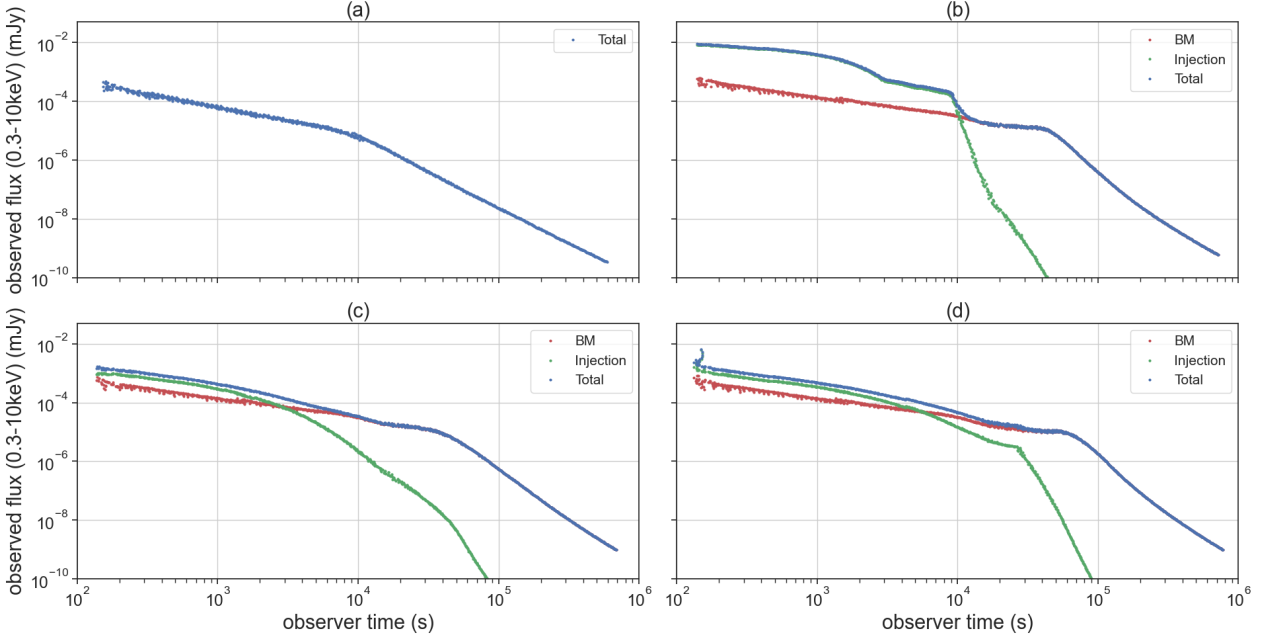


Figure 5. X-ray light curves with fluxes average over the (0.3 – 10)keV range for each simulation run at $z = 2.23$ and $d_l = 5.6 \times 10^{28}$ cm. (a) Shows the total observed flux for run 0. (b), (c), and (d) show the total observed flux and the contributions to the flux from the BM region and injection region for runs 1, 2, and 3, respectively.

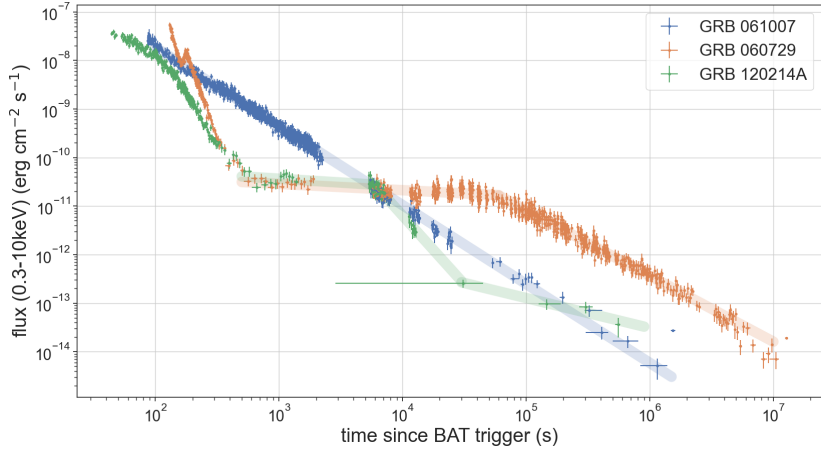


Figure 6. *Swift*-XRT light curves measured between 0.3-10keV for GRBs 061007 (blue), 060729 (orange), and 120213A (green). The faded lines show how the flux of each light curve decays with time according to a power law.

Table 2. Estimated start times (in seconds) for each of the phases of the light curves

Light curve	First plateau (s)	First decay (s)	Second Plateau (s)	Second Decay (s)
run 0 (one fit)	-	10^2	-	-
run 0 (two fits)	1×10^2	10^4	-	-
run 1	1×10^2	8×10^3	12×10^3	4×10^4
run 2	1×10^2	4×10^4	-	-
run 3	1×10^2	6×10^4	-	-
GRB 061007	-	1×10^2	-	-
GRB 060729	5×10^2	6×10^4	-	-
GRB 120213A	5×10^2	6×10^3	3×10^4	-

Table 3. Decay constants κ in each phase of the light curves. Error is given to 1 significant figure, arising from χ^2 fitting

Light curve	First plateau	First decay	Second Plateau	Second Decay
run 0 (one fit)	-	1.69 ± 0.01	-	-
run 0 (two fits)	0.918 ± 0.004	2.44 ± 0.001	-	-
run 1	1.00 ± 0.01	6.3 ± 0.01	0.57 ± 0.02	3.62 ± 0.01
run 2	0.969 ± 0.004	3.342 ± 0.005	-	-
run 3	0.936 ± 0.004	3.79 ± 0.01	-	-
GRB 061007	-	1.625 ± 0.005	-	-
GRB 060729	0.13 ± 0.02	1.356 ± 0.01	-	-
GRB 120213A	0.16 ± 0.05	2.8 ± 0.2	0.6 ± 0.1	-

the initial blast in the BM region. In runs 2 and 3, the merging of the FSs extends the plateau phase since the emission from the injection region decays more gradually. For runs 1 and 2, the final decay phase begins after the FSs fully merge, when the shock begins to decelerate. In run 3, the final decay phase starts slightly later since the slower decay rate of the engine means some energy continues to be delivered to the shocked region after the FSs have merged.

The light curve for run 0 figure 5 (a) was expected to be similar to GRB 061007 following a constant decay with no plateau. However, a switch from slow cooling (where $v'_c < v' < v'_m$) to fast cooling (where $v'_m, v'_c < v'$) for the observed frequency occurs around $t_{\text{obs}} \sim 1 \times 10^4$ s which splits the region into a shallower decay region and a steeper decay region. This results from a limitation in the emission model used, discussed in section 5. If, instead, the fit is taken across the entire light curve for run 0, then a decay rate in line with GRB 061007 is found instead (see table 3).

The light curves for runs 2 and 3 replicate the structure of GRB 060729 with a single plateau phase out to around $t_{\text{obs}} \sim 5 \times 10^4$ s before entering a final decay phase. This confirms that the dynamics of a spinning-down pulsar can replicate such GRBs. Additionally, the light curve for run 1 replicates the structure of GRB 120213A, with both having two independent plateau phases and a rapid decay in between. This suggests that the dynamics of a pulsar collapsing into a BH could be the origin of GRBs with these types of afterglows.

It is worth noting that although the general shape of the simulated light curves is reproduced, the exact power laws followed by the simulations appear to be steeper than in the observed GRBs. This might be explained in several ways, including limitations to the simulation and emission model discussed in section 5 or differences in the dynamics such as the total energy of the injection.

5. Additional Discussion

5.1. Limitations to simulations and their setup

The dynamical simulations and approach to energy injection successfully reproduced the self-similar profile discussed in vE14. Thus confirming this analytical description's validity when the injection follows an initial blast wave. Combined with the simplified emission model, this reproduced GRB light curves with plateau phases (runs 2 and 3) and second plateau phases (run 1) by considering different progenitor scenarios. However, these simulations are still subject to several limitations detailed here.

Firstly, simulations are run in 1D, ignoring lateral motion. In equation 15 a constant opening angle for the jet is assumed as it expands. Sideways spreading of the jet begins when causal contact is established among all angles of the collimated blast wave [25, 44]. For constant injection into a homogenous medium, vE14 calculates the onset of spreading at $\Gamma = 10$, meaning this assumption breaks down soon after the FSs merge. This may explain the difference in the final decay power law slopes between GRB 060729 and runs 2 or 3. In later works, spreading could be accounted for by finding the volume numerically in 2D simulations with GAMMA (assuming axial symmetry).

Secondly, runs 2 and 3 each demonstrate a gradual shutdown scenario for the spinning-down

pulsar with slightly differing approaches. Both runs recreated a similar afterglow, suggesting the long-lived RS in run 2 has little effect on its own and that either approach is a viable description of GRBs with a plateau. However, given the system's complexity, it would be beneficial to consider a more realistic shutdown by closely replicating the spin-down law of a magnetar [22].

Finally, the restricted number of simulations undertaken limits this study's ability to recreate the exact power laws of observed light curves as mentioned in section 4. Therefore, this work could be extended by reproducing the power laws present in GRBs 060729 and 120213 by altering the boundary conditions of the simulations.

5.2. Limitations to the emission model

The simplified emission model allowed the general features of the light curves, such as the plateau and decay phases, to be recreated with accurate timing. However, the model is limited in several ways discussed here, restricting the conclusions that can be drawn.

The most significant issue is the crude approximation of constant energy density, number density and Lorentz factor throughout the shocked region. This is confounded by the use of the global cooling approximation with $\epsilon_e = 0.1$, and $\epsilon_B = 0.01$ for all shocked regions. These approximations allow the general shape of the light curves to be calculated but ignore many of the specific details of the fluid profiles. This gives rise to the sudden switch from slow cooling to fast cooling in run 0, which is not present in observed GRBs. In future work, the GAMMA codes local cooling could be worked into the emission model, allowing local emissions to be considered. This would remove the crude averaging undertaken in shocked regions and allow the magnetic field generation efficiency ϵ_B to be considered at the FSs and RSs independently [32, 45, 46]. It would also eliminate the error introduced by equation 17, which neglects the difference in arrival time for emissions at varying radii.

Furthermore, the model only considers the simple case where the jet axis is aligned with the line of sight. Perturbed lines of sight are expected to change the timings of the light curves due to Doppler beaming but should not significantly impact their shape.

6. Conclusion

This paper presents numerical SRHD simulations of GRB blast waves followed by a relativistic pulsar wind in 1D. The moving-mesh code GAMMA improves resolution and efficiency compared to similar simulation codes [31]. To replicate several pulsar wind scenarios an injection of energy at the boundaries of the simulation was implemented. Four cases were simulated: no injection; constant injection followed by a rapid engine shutdown, replicating the collapse of the pulsar into a BH; constant injection with a tail region of decreasing Lorentz factor, approximating the gradual engine shutdown and introducing a long-lived reverse shock into the system [32, 33]; constant injection followed by a slow engine shutdown, again approximating the gradual engine shutdown.

The dynamical simulations showed a continuously decaying BM profile followed by a self-similar RS-CD-FS system discussed in vE14. After the engine shutdown is communicated to the RS, the RS-CD-FS system transitions into a second BM solution. This merges with the initial blast wave, forming a single BM solution that decays according to BM76.

A simplified emission model was presented and used to generate an X-ray light curve for each simulation. The dynamics of the simulations were used to justify the features of these light curves. They were then compared with a sample of observed light curves from the *Swift*-XRT dataset, confirming their similarities. This provides a possible description of the dynamics for afterglows with a plateau and those with a secondary plateau.

This study is limited primarily by the simplified emission model and its 1D nature. The use of GAMMA allows for a straightforward progression of the study utilizing its two-dimensional simulations and local cooling treatment. Additionally, a study designed to reproduce the power laws of observed light curves might further confirm the applicability of this scenario.

Acknowledgements

I wish to thank my MPhys project supervisor, Dr Hendrik van Eerten, and co-supervisor, Dr Sayan Kundu, for providing invaluable guidance throughout the project. I also want to thank my MPhys project partner, Mr Christopher Hilton, with whom I have closely collaborated throughout the project.

References

- [1] Woosley S E 1993 *ApJ* **405** 273
- [2] Paczyński B 1998 *ApJL* **494** L45–8
- [3] MacFadyen A I and Woosley S E 1999 *ApJ* **524** 262–89
- [4] Eichler D, Livio M, Piran T and Schramm D N 1989 *Nature* **340** 126–8
- [5] Mochkovitch R, Hernanz M, Isern J and Loiseau S 1995 *Astron. Astrophys.* **293** 803–9
- [6] Abbott B P *et al.* 2017 *Phys. Rev. Lett.* **119**(16) 161101
- [7] Abbott B P *et al.* 2017 *ApJL* **848** L12
- [8] Zhang B, Lü HJ and Liang EW 2016 *Space Sci Rev* **202** 3–32
- [9] Mészáros P and Rees M J 1997 *ApJ* **476** 232–7
- [10] Kobayashi S, Piran T and Sari R 1999 *ApJ* **513** 669
- [11] Meszaros P, Laguna P and Rees M J 1993 *ApJ* **415** 181
- [12] Piran T, Shemi A and Narayan R 1993 *MNRAS* **263** 861
- [13] Kobayashi S, Piran T and Sari R 1997 *ApJ* **490** 92
- [14] Daigne F and Mochkovitch R 1998 *MNRAS* **296** 275–86
- [15] Blandford R D and McKee C F 1976 *Phys. Fluids* **19** 1130–8
- [16] Pe'er A and Zhang B 2006 *ApJ* **653** 454–61
- [17] Nakar E and Granot J 2007 *MNRAS* **380** 1744–60
- [18] Blandford R D and McKee C F 1977 *MNRAS* **180** 343–71
- [19] Gehrels N *et al.* 2004 *ApJ* **611** 1005–20
- [20] Nousek J A *et al.* 2006 *ApJ* **642** 389–400
- [21] Zhang B, Fan Y Z, Dyks J, Kobayashi S, Mészáros P, Burrows D N, Nousek J A and Gehrels N 2006 *ApJ* **642** 354–70
- [22] Zhang B and Mészáros P 2001 *ApJL* **552** L35–8
- [23] Du M, Yi S X, Liu T, Song C Y and Xie W 2021 *ApJ* **908** 242
- [24] Stratta G, Dainotti M G, Dall'Osso S, Hernandez X and Cesare G D 2018 *ApJ* **869** 155
- [25] van Eerten H 2014 *MNRAS* **442** 3495–510
- [26] Butler N R and Kocevski D 2007 *ApJ* **668** 400
- [27] Metzger B D, Giannios D, Thompson T A, Bucciantini N and Quataert E 2011 *MNRAS* **413** 2031–56
- [28] Zhang D and Dai Z 2009 *ApJ* **703** 461
- [29] Zhang D and Dai Z G 2010 *ApJ* **718** 841–66
- [30] Dai Z G, Wang X Y, Wu X F and Zhang B 2006 *Sci* **311** 1127–9
- [31] Ayache E H, van Eerten H J and Eardley R W 2022 *MNRAS* **510** 1315–30
- [32] Ayache E H, van Eerten H J and Daigne F 2020 *MNRAS* **495** 2979–93
- [33] Lamberts A and Daigne F 2018 *MNRAS* **474** 2813–27
- [34] Mignone A and Bodo G 2006 *MNRAS* **368** 1040–54
- [35] Wijers R A M J, Rees M J and Mészáros P 1997 *MNRAS* **288** L51–6
- [36] Mészáros P, Rees M J and Wijers R A M J 1998 *ApJ* **499** 301
- [37] Sari R, Piran T and Narayan R 1998 *ApJL* **497** L17–20
- [38] Granot J, Piran T and Sari R 1999 *ApJ* **513** 679
- [39] Wijers R A M J and Galama T J 1999 *ApJ* **523** 177–86
- [40] Curran P A, Starling R L C, van der Horst A J and Wijers R A M J 2009 *MNRAS* **395** 580–92
- [41] van Eerten H, Zhang W and MacFadyen A 2010 *ApJ* **722** 235–47
- [42] Wang X G, Zhang B, Liang E W, Lu R J, Lin D B, Li J and Li L 2018 *ApJ* **859** 160
- [43] Evans P A *et al.* 2009 *MNRAS* **397** 1177–201
- [44] van Eerten H and MacFadyen A 2013 *ApJ* **767** 141
- [45] Beniamini P and van der Horst A J 2017 *MNRAS* **472** 3161–8
- [46] Santana R, Duran R B and Kumar P 2014 *ApJ* **785** 29